



# Mesoporous carbon@silicon-silica nanotheranostics for synchronous delivery of insoluble drugs and luminescence imaging

Qianjun He, Ming Ma, Chenyang Wei, Jianlin Shi\*

State Key Laboratory of High Performance Ceramics and Superfine Microstructure, Shanghai Institute of Ceramics, Chinese Academy of Sciences, 1295 Ding-Xi Road, Shanghai 200050, China

## ARTICLE INFO

### Article history:

Received 29 November 2011  
Accepted 22 February 2012  
Available online 16 March 2012

### Keywords:

Mesoporous silica  
Nanoparticle  
Hierarchical nanostructures  
Drug delivery  
Luminescence imaging  
Theranostic nanomedicine

## ABSTRACT

A hierarchical theranostic nanostructure with carbon and Si nanocrystals respectively encapsulated in the mesopores and within the framework of mesoporous silica nanoparticles (CS-MSNs) was constructed by a bottom-up self-assembly strategy combining an *in situ* one-step carbonization/crystallization approach. CS-MSNs exhibited narrow size distribution, high payload of insoluble drugs and unique NIR-to-Vis luminescence imaging feature. The bio-conjugated CS-MSNs with a PEGylated phospholipid compound and hyaluronic acid showed excellent dispersivity and could specifically target cancer cells overexpressing CD44, deliver insoluble drugs into these cells and consequently kill them effectively, and also fluorescently image them simultaneously in a unique and attractive NIR-to-Vis luminescence imaging fashion, providing a promising opportunity for cancer theranostics.

© 2012 Elsevier Ltd. All rights reserved.

## 1. Introduction

According to the specific needs for the treatment of major diseases (typically cancers and cardiovascular diseases), such as i) the early detection and diagnosis, ii) the targeted delivery of therapeutic agents, and iii) the synchronous monitoring of therapeutic responses, the “theranostic” concept has been introduced in clinics to combine diagnostic and therapeutic capabilities into a single agent. The occurrence of nanotechnology has offered a number of advanced nano-platforms with combined imaging and therapeutic functions. Subsequently, “theranostic nanomedicine”, integrating the virtues of advanced imaging and therapeutic nano-platforms, is rapidly growing into a promising medical methodology, and has drawn much attention in the past few years [1–3]. Great efforts have been devoted toward theranostic nanomedicine, however there are still challenges in increasing the payload of specific therapeutic agents, typically water-insoluble drugs, improving the imaging quality, enhancing the targetability, etc.

Mesoporous silica nanoparticles (MSNs) have been qualified as a new type of excellent theranostic nano-platform, thanks to their unique features, such as tunable porosity, high surface area, large pore volume, facile functionalization, good biocompatibility, high physicochemical and biochemical stability, etc [4–6]. A broad range

of imaging and therapeutic agents, such as superparamagnetic iron oxide nanoparticles, quantum dots, upconversion nanoparticles, Gd complexes, fluorescein molecules, genes, chemotherapeutic drugs, and so on, have been loaded/grafted/encapsulated into MSNs to achieve theranostic purposes [7–13]. However, as far as drug loading is concerned, the loading capacity of MSNs for water-insoluble anti-cancer drugs, which can be hardly loaded into hydrophilic pore network of MSNs, should be greatly enhanced for the effective drug delivery, because about 40% of anti-cancer drugs are hydrophobic but frequently more effective than the others.

Biological optical imaging is one of the most common imaging modalities for disease diagnosis. The present organic fluorescent dyes or most of luminescent quantum dots containing heavy metal ion(s) as bio-imaging agents have poor biochemical stability or potential toxicity, respectively. Upconversion nanoparticles (UCNPs) usually containing rare-earth heavy elements and exhibiting outstanding upconversion luminescence have been developed for applications in biological imaging and drug delivery [14–18]. However comparatively, Si nanocrystals are more biodegradable and non-cytotoxic because of absence of heavy elements and non-toxicity of degradation products [19], and also have been recently discovered capable of luminescence in the visible region through the multi-photon excitation of near infrared (NIR) light, which is highly desired in medical imaging to avoid the photo-damage and the disturbance by tissue autoluminescence [20,21]. Therefore, the combination of MSNs with Si nanocrystals would be a highly promising theranostic platform, which, however, has never been

\* Corresponding author. Tel.: +86 21 52412714; fax: +86 21 52413122.  
E-mail address: [jlshi@sunm.shcnc.ac.cn](mailto:jlshi@sunm.shcnc.ac.cn) (J. Shi).

reported before as far as we know, largely because of the difficulties and complexity in assembling MSNs with Si nanocrystals.

In addition, the refined active targeting is still a pressing challenge to theranostic MSNs, though the passive targeting is easily available owing to the enhanced permeability and retention (EPR) effect of abnormal tumors [22]. Limited efforts have been made for the active targeting of MSNs by conjugating tumor-recognition molecules such as folate, antibodies, mannose [23–26].

Herein, we develop a facile bottom-up self-assembly strategy to synthesize a kind of oxygen-deficient MSNs, followed by an *in situ* one-step carbonization/crystallization strategy to efficiently construct a type of theranostic hierarchical nanostructure with carbon encapsulated in the mesopores and Si nanocrystals embedded within the mesoporous wall of MSNs, respectively (abbreviated as ‘CS-MSNs’), as shown in Scheme 1. It is important to note that the *in situ* encapsulation of carbon in the mesopores is expected to remarkably increase the payload of water-insoluble drugs such as typical hydrophobic anti-cancer drug camptothecin (CPT), and Si nanoparticles crystallized *in situ* within the mesoporous wall are expected to create a kind of NIR-to-Vis luminescence while will not affect the mesoporous structure. Furthermore, the bio-conjugation with a PEGylated phospholipid compound DSPE-PEG and a natural mucopolysaccharide hyaluronic acid (HA) are employed to improve the aqueous solubility of the CPT-loaded CS-MSNs and endow CS-MSNs with the capabilities of the targeted drug delivery. As expected, the bio-conjugated CS-MSNs (CS-MSNs-DSPE-PEG-HA) will be used as a new type of theranostic nano-platform capable of the high-capacity loading and targeted delivery of water-insoluble drug molecules into special cancer cells, consequently able to selectively kill them under the synchronous monitoring by the NIR-to-Vis luminescence imaging.

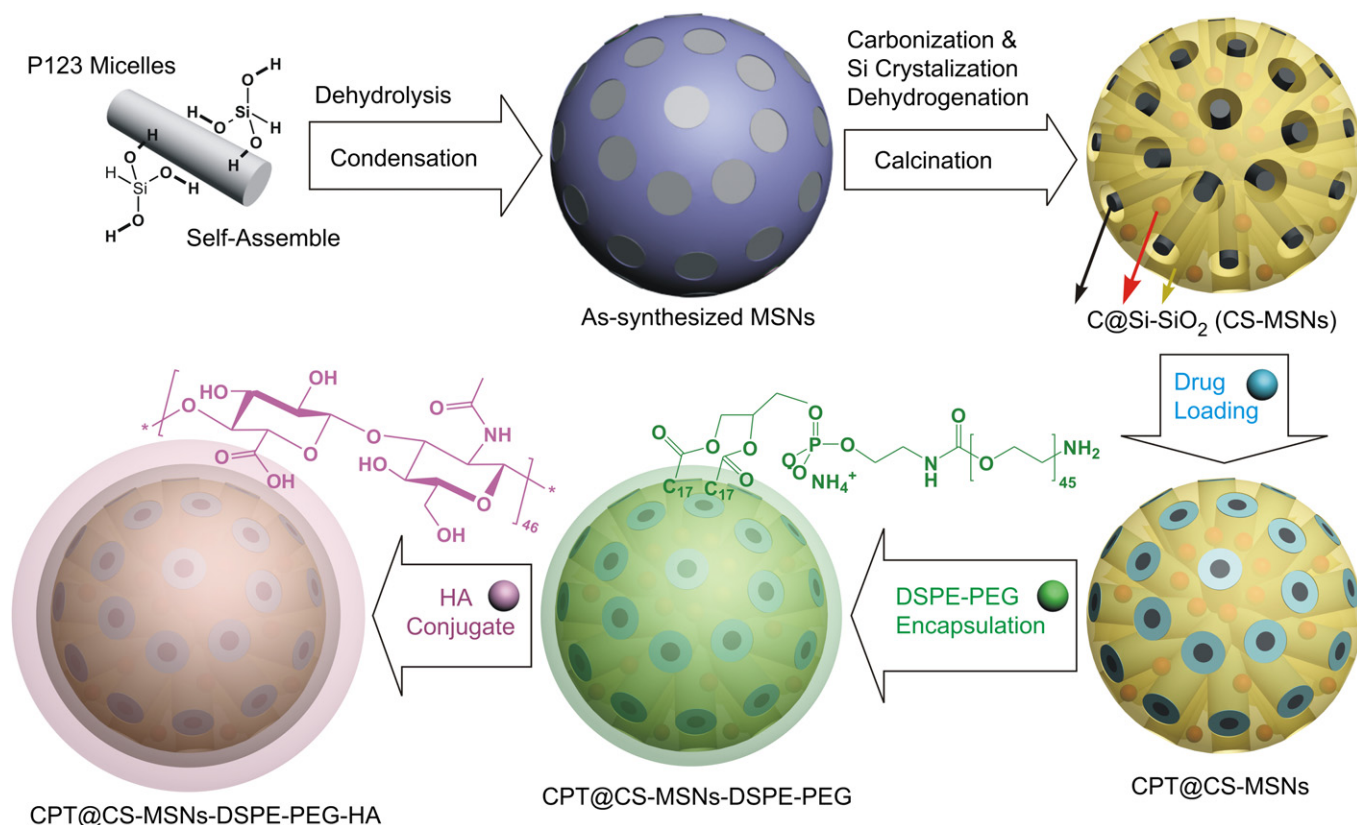
## 2. Materials and methods

### 2.1. Synthesis of CS-MSNs

Firstly, Pluronic P123 (3.4 g, PEO<sub>20</sub>PPO<sub>70</sub>PEO<sub>20</sub>, BASF Co., Ltd.) and NaCl (6 g, Sinopharm Chemical Reagent Co. Ltd., Shanghai) were fully dissolved into a HCl solution (100 mL, 0.1 M) at 35 °C under intensive stirring and under argon blowing protection. Then triethoxysilane (9 mL, TES, Alfa Aesar) was added dropwise. The reaction was carried out in a glove box to avoid the potential hazard of TES [27]. After 12 h, the reaction solution in a colloidal state was centrifuged for 10 min with the centrifugal force of 18,000 g in a high speed refrigerated centrifuge, and washed for three times with deionized water to remove residual reactants. The collected as-synthesized oxygen-deficient mesoporous silica nanoparticles (MSNs) were dispersed in deionized water and then the freeze drying power was collected in order to reduce the aggregation of nanoparticles. Finally, the freeze drying power was calcined for 3 h at 900 °C at a heating rate of 2 °C min<sup>-1</sup> under nitrogen protection to obtain the black product CS-MSNs. A small part of large particles were filtered off with 0.45 μm Millex-HP Filter Unit (Millipore Express® PES Membrane, Millipore Ireland Ltd.).

### 2.2. Insoluble drug loading with CS-MSNs

A vacuum/ultrasound-assisted nanocasting method [28] was used to load a typical water-insoluble anti-cancer drug, camptothecin (CPT, Beijing HuaFeng United Technology Co., Ltd., Beijing). Initially, CS-MSNs were dried 12 h at 120 °C in vacuum, and then further kept in nitrogen gas at room temperature for 2 h. Then CPT (10 mg) was completely dissolved into dry DMSO (10 mL) in assistance of ultrasound. Dry CS-MSNs (40 mg) was added into the CPT solution, and mixed for 30 min under vacuum, ultrasound and light-sealed conditions. Finally, the CPT-loaded CS-MSNs (CPT@CS-MSNs) was collected by high speed refrigerated centrifugation, and then washed for three times with pH = 7.4 phosphate buffered saline (PBS, Beijing Zoman Biotechnology Co., Ltd., Beijing) to remove the residual DMSO. The CPT@CS-MSNs is hardly suspensible in water owing to strong hydrophobic property. The UV adsorption spectra of the initial CPT solution before adding CS-MSNs and the upper clear solution after CPT loading and centrifugation were collected on a Shimadzu UV-3101PC UV–vis absorption spectrophotometer. According to the absorbance difference, the CPT loading capacity of CS-MSNs was calculated to be 68 mg g<sup>-1</sup> by the Beer–Lambert law.



**Scheme 1.** Schematic illustration for the synthesis, drug loading, and bio-conjugation of CS-MSNs.

### 2.3. Bio-conjugate chemistry of CS-MSNs

CPT@CS-MSNs (40 mg) was dispersed in the chloroform solution (16 mL, 1 mg mL<sup>-1</sup>) of 1,2-distearoyl-sn-glycero-3-phosphoethanolamine-N-[amino(polyethylene glycol)-2000] ammonium salt (DSPE-PEG2000-Amine, Avanti Polar Lipids, Inc., Alabama) under ultrasound assistance. The mixture was vacuumized slowly at room temperature for 3 h to remove the solvent, then redispersed in PBS and washed for several times to remove the residual DSPE-PEG2000-Amine. The DSPE-PEG2000-Amine-coated CPT@CS-MSNs (CPT@CS-MSNs-DSPE-PEG) is well suspendible in water.

Hyaluronic acid (HA, molecular weight = 18 kDalton, 21 mg mL<sup>-1</sup>, 5 mL, Zhenjiang Dong Yuan Biotech Co., Ltd., Zhenjiang) was activated with N-hydroxysuccinimide (6.8 mg, NHS, Sinopharm Chemical Reagent Co. Ltd., Shanghai) and 1-Ethyl-3-[3-dimethylaminopropyl] carbodiimide hydrochloride (11.3 mg, EDC, Alfa Aesar) for 20 min, and then the aqueous solution of CPT@CS-MSNs-DSPE-PEG (2 mL) was added dropwise under intensive stirring. The mixed solution was kept overnight at room temperature. Finally, the HA-conjugated CPT@CS-MSNs-DSPE-PEG (CPT@CS-MSNs-DSPE-PEG-HA) was collected by high speed refrigerated centrifugation, and washed several times with deionized water to remove the residual reactants, and sealed in brown bottles and stored at 4 °C.

### 2.4. Characterization of materials

The morphology and mesostructure of nanoparticles were observed via transmission electron microscopy (TEM). TEM micrographs were obtained on a JEM-2010 electron microscope with an accelerating voltage of 200 kV. Meanwhile, energy dispersive spectra (EDS) were collected on observed nanoparticles, and high-resolution TEM images (HR-TEM) and selected area electron diffraction (SAED) patterns were also collected. The mesostructure ordering was characterized by small-angle X-ray diffraction (SA-XRD). SA-XRD data were recorded on Rigaku D/Max-2550 V diffractometer using Cu K $\alpha$  radiation (40 kV and 40 mA) at a scanning rate of 0.4° min<sup>-1</sup> over the range of 0.5–6.0° with a step width of 0.002°. The porosity was measured by nitrogen adsorption–desorption isotherm experiments, which were carried out on a Micromeritics Tristar 3000 analyzer at 77 K under a continuous adsorption condition, with all samples dried for 12 h at 120 °C under nitrogen before measurements. Average pore diameter was calculated from desorption branches of the nitrogen adsorption–desorption isotherms by the Barrett–Joyner–Halenda (BJH) method, and specific surface area and pore volume were calculated by Brunauer–Emmett–Teller (BET) and BJH methods, respectively. The particle size distribution data and zeta potential values of nanoparticles were collected by a DLS method in a Zetasizer nano ZS90 analyzer (Malvern Instruments Ltd., UK). The carbon content of CS-MSNs was measured by CHN elemental analyses (Vario MICRO, Elementar Analysensysteme GmbH, Germany). To determine the chemical valences of carbon and silicon, X-ray photoelectron spectroscopy (XPS) were collected on a VG Micro MKII instrument using monochromatic Al K $\alpha$  X-rays. Samples were adequately dewatered in ultra-high vacuum before XPS measurements. FTIR spectra were collected on a Nicolet (Madison, WI) Magna 550 infrared spectrophotometer using KBr technique. Three hundred scans were collected per sample over the range of 4000–400 cm<sup>-1</sup> at a resolution of 4 cm<sup>-1</sup>. Raman spectra were recorded on a laser Raman spectroscope (JobinYvon LabRAM HR800) with a 532 nm diode laser at room temperature. Multi-photon photoluminescence spectra of CS-MSNs in ethanol were recorded on a FluoroLog-3 Spectrofluorometer (Jobin Yvon, France), under the excitation of a 980 nm semiconductor laser with 470 mW of power and 1.6 W cm<sup>-2</sup> of power density. Single-photon photoluminescence spectra of CS-MSNs in ethanol were collected under 245 nm and 327 nm excitations on a Shimadzu RF-5301PC Spectrofluorophotometer (Shimadzu Co., Japan) using a Xe lamp as excitation source.

### 2.5. Cytotoxicity evaluation

Representative normal and cancer cells, fibroblast L929 cells and breast cancer MCF-7 and MDA-MB-468 cells, were respectively cultivated in the DMEM culture medium (GIBCO, New York) containing 10% fetal bovine serum (FBS, Sijiqing Biological Engineering Materials Co., Ltd., Hangzhou). All cells were maintained at 37 °C in a humidified and 5% CO<sub>2</sub> incubator. For all experiments, cells were harvested by the use of 0.25% trypsin (Sigma) in D-Hank's solution (0.40 g KCl, 0.06 g KH<sub>2</sub>PO<sub>4</sub>, 8.00 g NaCl, 0.35 g NaHCO<sub>3</sub>, 0.048 g Na<sub>2</sub>HPO<sub>4</sub>, 1000 mL H<sub>2</sub>O) and resuspended in fresh medium before plating. *In vitro* cytotoxicity was assessed by the standard Cell Counting Kit-8 (CCK-8, Beyotime Institute of Biotechnology, Jiangsu) assay. The statistical evaluation of data was performed using a two-tailed unpaired Student's *t*-test. A *p*-value of less than 0.05 was considered statistically significant. Each data point is represented as mean  $\pm$  standard deviation (SD) of eight independent experiments (*n* = 8, *n* indicates the number of wells in a plate for each experimental condition). The dose dependence of the cytotoxicity was investigated at different particle concentrations (5–80  $\mu$ g mL<sup>-1</sup>).

Cells were seeded in 96-well plates (Corning Inc., New York) at a density of  $2 \times 10^4$  cells per well. After incubation for 24 h at 37 °C in 100  $\mu$ L culture medium containing 10% FBS, culture medium was discarded and then cells were treated with 100  $\mu$ L pH 7.4 D-Hank's solution of samples at different concentrations. After

incubation for 24 h, 10  $\mu$ L of CCK-8 solution was added. After another 4 h, the absorbance was monitored at 450 nm on a micro-plate reader (Bio-Tek ELx800). A culture medium without the addition of nanoparticles was used as the blank control. A culture medium with the addition of nanoparticles at corresponding concentrations but no addition of CCK-8 solution was used as the background needing to be subtracted for eliminating the luminescence interference of samples. The cytotoxicity was expressed as the percentage of the cell viability as compared with the blank control.

### 2.6. Assay for CD44 expressed on cells

CD44 was quantitatively detected by an enzyme-linked immunosorbent assay using an ELISA kit (Bio-Swamp Life Science Co.). L929, MCF-7 and MDA-MB-468 cells at the same density were dispersed into PBS respectively, and sonicated/disrupted thoroughly to solubilize CD44. The CD44 assay followed the manufacturer's protocol. All assays were performed in duplicate. The absorbance of each micro-well was read on the micro-plate reader using 450 nm as the primary wavelength. A linear standard curve was generated by plotting the average absorbance on the vertical axis versus the corresponding CD44 standard concentration on the horizontal axis. The concentration of soluble CD44 in each sample was determined by using the standard curve.

### 2.7. Intracellular targeted delivery and synchronous luminescence imaging of live cells

MDA-MB-468 cells, MCF-7 cells and L929 cells (10<sup>5</sup> cells per dish) were seeded in coverglass bottom dishes (35  $\times$  10 mm, Corning Inc., New York), respectively, and then treated with CPT@CS-MSNs-DSPE-PEG-HA at the same final concentration of 80  $\mu$ g mL<sup>-1</sup> for 4 h, respectively. Then the culture medium was discarded, and cells were washed adequately for several times with D-Hank's solution to remove the residual nanoparticles, and then directly visualized for the intracellular internalization and drug delivery/release of CPT@CS-MSNs-DSPE-PEG-HA and the NIR-to-Vis luminescence imaging of live cells under an Olympus FV1000-IX81 laser scanning confocal microscope (LSCM) equipped with a 980 nm semiconductor laser. UV and NIR light resources with excitation lengths of 405 nm and 980 nm were used to excite cells treated with nanomaterials, and corresponding fluorescence signals of blue and yellow channels (410–450 nm and 550–650 nm, respectively) were detected to determine CPT and CS-MSNs, respectively. Further, cellular profiles were collected by linear scanning to localize nanoparticles more clearly. Meanwhile, bright field images were also collected. In the assay, all experiments were carried out under a light-sealed condition to avoid photo-bleaching.

## 3. Results and discussion

### 3.1. Synthesis and characterization of CS-MSNs

As illustrated by Scheme 1, the oxygen-deficient MSNs were synthesized by using Pluronic P123 as a structure-directing agent (SDA) and triethoxysilane (TES) as a special silicon source by a bottom-up self-assembly route, as reported previously by us [29]. After the removal of P123 through the solvent extraction followed by the dehydrogenation between O<sub>3</sub>Si–H terminal groups through post-calcination at 600 °C, copious oxygen vacancies were created, which endowed the oxygen-deficient MSNs (ODL-MSNs) with the defect-related UV-to-Vis luminescence features in favor of cell imaging [29]. However, the special application of ODL-MSNs in cancer theranostics might be limited to a certain extent because of the UV photo-damage and the disturbance by tissue autoluminescence. Therefore, the superior NIR-to-Vis luminescence feature is highly desired for bio-imaging. In this investigation, we try to create Si nanocrystals within the oxygen-deficient network of ODL-MSNs while maintaining the mesostructure structure of MSNs, because Si nanocrystals have been proved to possess good biocompatibility and NIR-to-Vis luminescence feature recently [20,21]. However, Si nanocrystals can only be created by calcination at temperatures significantly higher than 600 °C, at which, unfortunately, the mesoporous structure of ODL-MSNs would collapse severely [29].

In this work, we discovered that high temperature calcination (900 °C) under inert atmosphere can simultaneously create Si nanocrystals in the mesoporous framework and protect the mesoporous structure from collapse. In the meantime, very

fortunately, the P123 micelles within the mesopores of MSNs were *in situ* carbonized, which supported the mesostructure from collapse and make the prepared CS-MSNs become hydrophobic due to the generation of carbon in the mesopore channels in high favor of the adsorption/loading of water-insoluble drugs such as CPT, as illustrated by Scheme 1.

The morphology and mesostructure of the as-synthesized MSNs and CS-MSNs were characterized with TEM (Fig. 1a). It can be found from the TEM images that the as-synthesized MSNs possess uniform particle size of about 220 nm, spherical morphology and well-defined mesoporous structure. After calcination at 900 °C, both spherical morphology and mesoporous structure were well maintained of CS-MSNs (Fig. 1b). Moreover, the well-defined small-angle X-ray diffraction (SA-XRD) peak at 0.6–0.8° (Fig. 2a) also indicated that both the as-synthesized MSNs and CS-MSNs possess partially ordered mesoporous structures. If P123 was removed by solvent extraction before calcination, the mesoporous structure of MSNs would be destroyed after post-calcination at temperatures of above 600 °C, as shown previously by us [29]. Therefore it is thought that the *in situ* carbonization of P123 micelles within the mesopores is of great benefit to support the mesoporous structure. In addition, it could be found from the small-angle XRD peak shift toward high angle that the mesopore interspace became smaller after calcination, which could result from the shrinkage of mesoporous walls during dehydrogenation.

It is worth noting that large numbers of Si nanocrystals of about 3 nm in diameter were crystallized within the mesoporous walls during high temperature treatment, as indicated by the clear (311) lattice fringes of the diamond cubic Si phase with a (311)

interplanar spacing of 0.16 nm in high-resolution TEM (HR-TEM) image (Fig. 1c) and the corresponding selected area electron diffraction (SAED) pattern (inset of Fig. 1c) [30]. Although it is difficult to exclude the possibility of Si nanocrystals' segregation out of the mesopore walls, however, as Si nanocrystals were derived from the *in situ* crystallization from silica network during post-calcination which was confirmed by Raman and FTIR analyses, Si nanocrystals should be mostly embedded within the framework, as proved by the visible lattice fringes of Si nanocrystals locating in the mesopore framework in the HR-TEM image (Fig. 1c). Furthermore from wide-angle XRD patterns (Fig. 2b), it could also be found that there are two broad diffraction peaks of CS-MSNs at 28.5° and 47.2°, which can be indexed as (111) and (220) planes of cubic Si (JCPDF card No. 27-1402), respectively, and the wide peaks also suggest the small particle size of Si nanoparticles. In addition, both the as-synthesized MSNs and CS-MSNs exhibited a wide diffraction peak at 22.4°, which should be assigned to amorphous silica.

In order to investigate the P123 carbonization and the Si crystallization within MSNs, the Raman and FTIR spectra of the as-synthesized MSNs and CS-MSNs were collected, as shown in Fig. 3. It could be found clearly that the as-synthesized MSNs exhibited an especially strong Raman peak at 2262 cm<sup>-1</sup> (Fig. 3a), which is readily assigned to the Si–H stretching vibration [31,32]. Correspondingly, the as-synthesized MSNs also showed two characteristic FTIR absorption bands of Si–H at 2252 cm<sup>-1</sup> and 880 cm<sup>-1</sup> (Fig. 3b), corresponding to Si–H stretching and bending vibrations, respectively [33]. This indicated that high concentrations of O<sub>3</sub>Si–H terminal groups had been kept successfully during

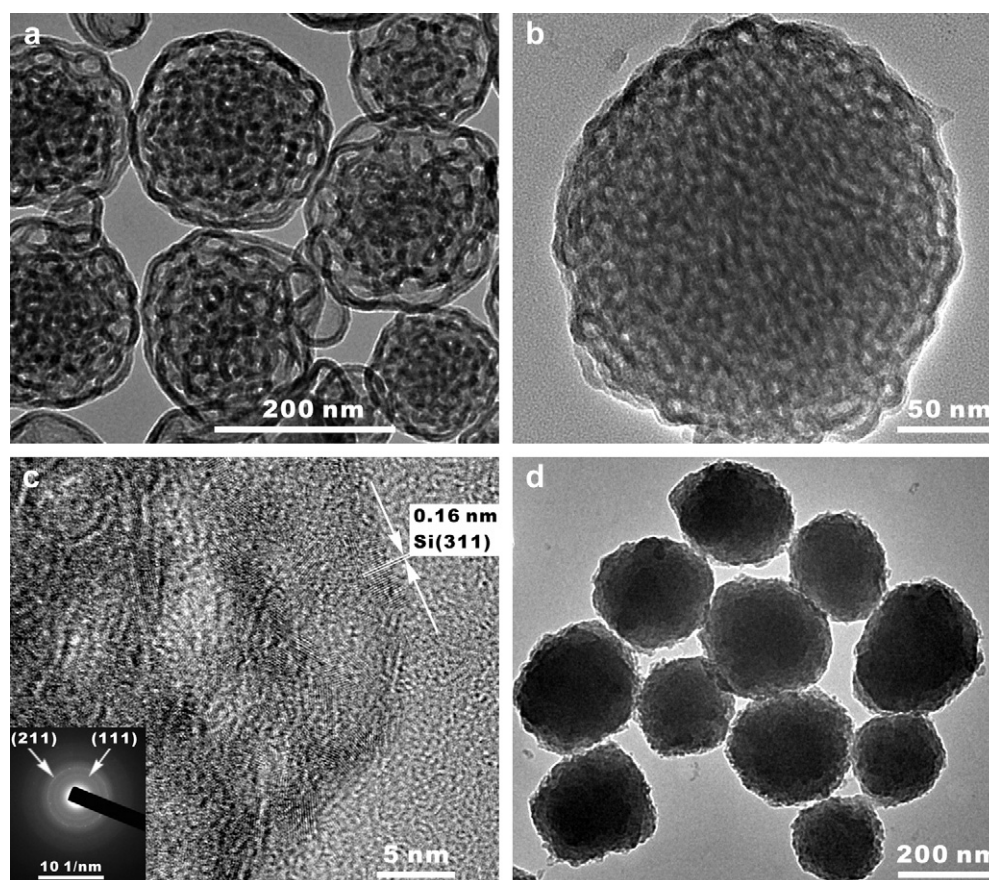


**Fig. 1.** TEM images of the as-synthesized MSNs (a), CS-MSNs (b, c), and CPT@CS-MSNs-DSPE-PEG-HA (d). Figure c is an HR-TEM image of CS-MSNs, and the inset is the corresponding SAED pattern.

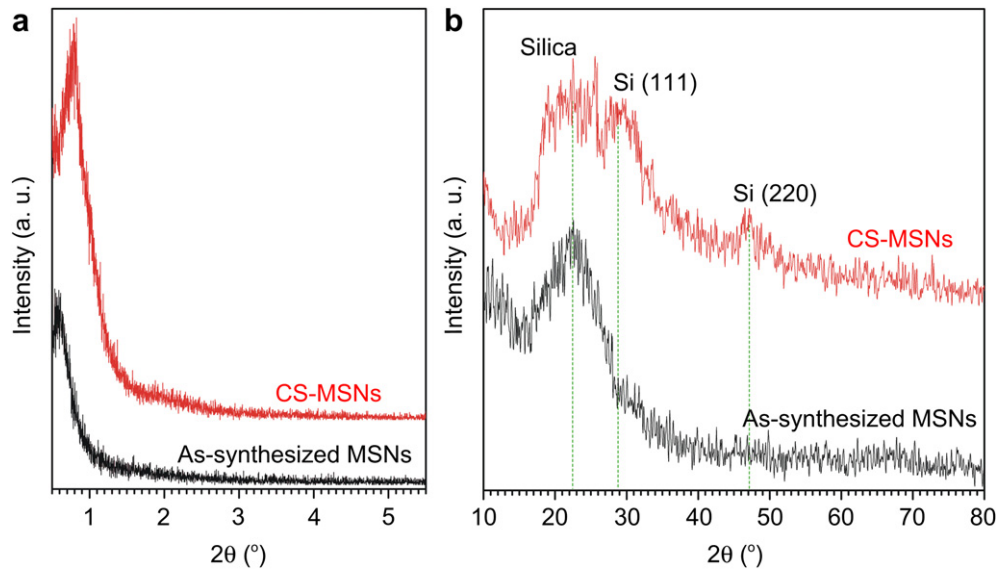


Fig. 2. Small-angle (a) and wide-angle (b) XRD patterns of the as-synthesized MSNs and CS-MSNs.

the hydrolysis and condensation of TES [32], owing to the mild reaction conditions and inert atmosphere protection from air oxidation of  $O_3Si-H$  groups into  $O_3Si-OH$  as described in Materials and Methods. After calcination at  $900^\circ C$  under nitrogen protection, the Si-H stretching and bending vibration bands in Raman and FTIR spectra disappeared, however there was a new and broadened Raman band centered at  $480\text{ cm}^{-1}$  of CS-MSNs, which can be attributed to the Si-Si stretching vibration mode of Si nanocrystals of small particle size with a shifting toward lower frequency compared with bulk silicon ( $520\text{ cm}^{-1}$ ) [34,35]. This suggested the dehydrogenation between  $O_3Si-H$  terminal groups and the consequent Si crystallization from silica network during post-calcination. Moreover, a characteristic absorption band of Si-OH at  $950\text{ cm}^{-1}$  also disappeared after calcination at  $900^\circ C$ , indicating that the Si-O-Si network further condensed via the dehydration between Si-OH groups. In addition, several characteristic FITC adsorption bands of P123 encapsulated within MSNs at

$2980\text{--}2850\text{ cm}^{-1}$  and  $1460\text{--}1378\text{ cm}^{-1}$ , corresponding to  $CH_3/CH_2$  stretching and bending vibrations, respectively, also remarkably weakened or even disappeared after calcination at  $900^\circ C$  under nitrogen flow protection (Fig. 3b), reflecting the carbonization of P123. Furthermore, CS-MSNs distinctly showed two characteristic Raman bands of graphite-like carbon at  $1560\text{ cm}^{-1}$  (G band) and  $1300\text{ cm}^{-1}$  (D band), as shown in Fig. 3a, also indicating the carbonization of P123 in CS-MSNs. The carbon content of CS-MSNs was measured to be 11.3 wt.%. Moreover, both zero-valent carbon and silicon are detectable on CS-MSNs state by XPS, as shown by Fig. S1 in the Supporting information, which further proves carbonization and Si crystallization in CS-MSNs.

Nitrogen adsorption-desorption measurement was used to investigate the porosity of samples. As shown in Fig. 4, both the as-synthesized MSNs and CS-MSNs exhibited the classical type-IV adsorption-desorption isotherms of mesoporous materials. Furthermore, the adsorption-desorption isotherms of the as-

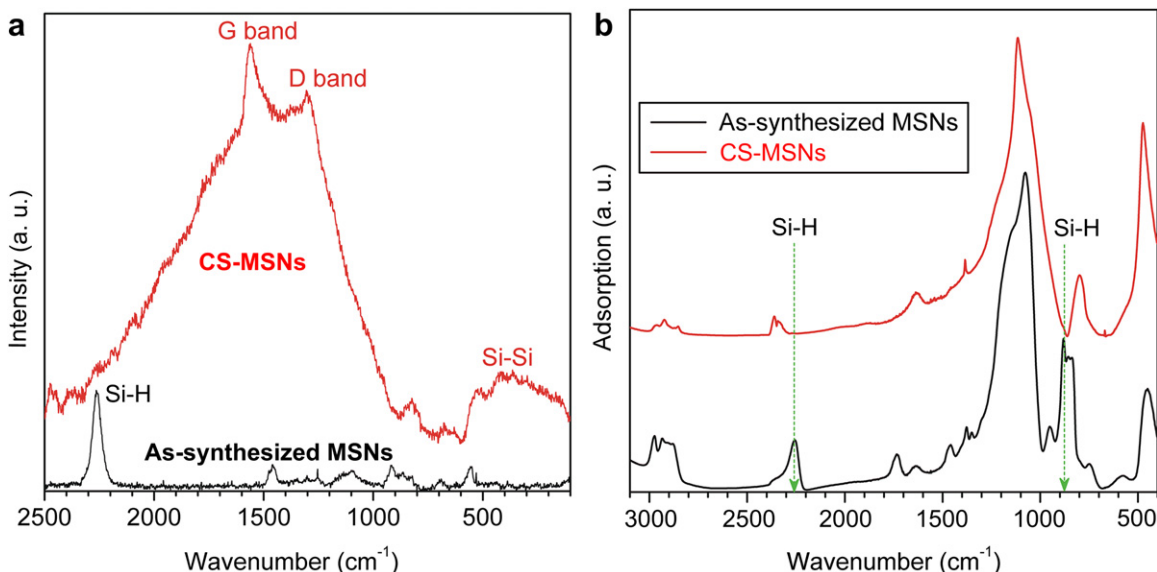


Fig. 3. Raman (a) and FTIR (b) spectra of the as-synthesized MSNs and CS-MSNs.

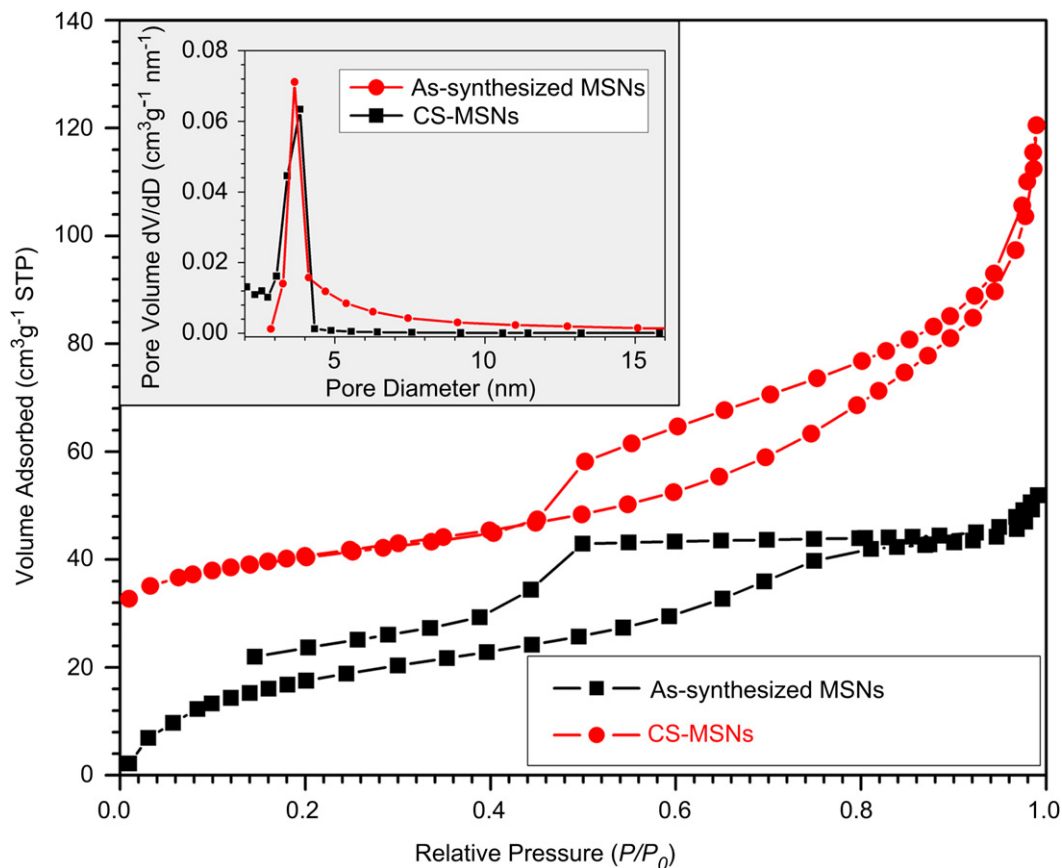


Fig. 4. Nitrogen adsorption–desorption isotherms and pore size distribution curves (inset) of the as-synthesized MSNs and CS-MSNs.

synthesized MSNs have a type-H2 hysteresis loop, suggesting the pore channels were partially blocked up by P123. However, the adsorption–desorption isotherms of CS-MSNs have a type-H3 hysteresis loop, which indicates that CS-MSNs have a kind of slit-like pore structure. Such slit-like pore channels were believed to be constructed from the mesopores of silica and the encapsulated

carbon, as shown by the hierarchical structure of CS-MSNs in Scheme 1. In addition, there are also well-defined step loops at the relative pressures of 0.4–0.6, which suggests that they possess uniform mesoporous structures in accordance with the results obtained from TEM images (Fig. 1) and small-angle XRD data (Fig. 2a). Furthermore, it can be found that CS-MSNs have slightly

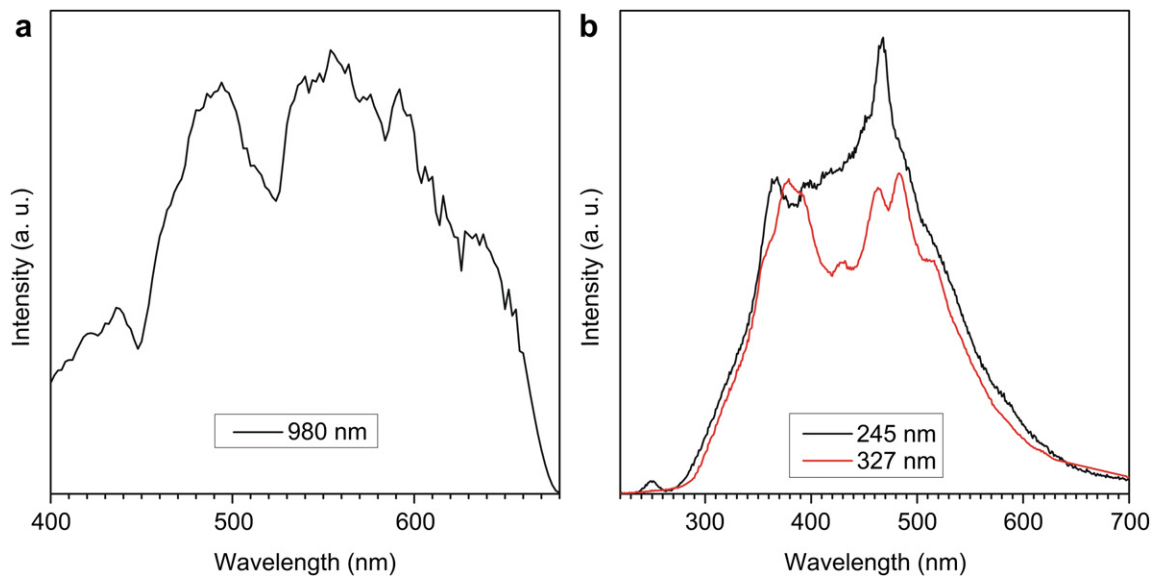


Fig. 5. NIR-to-Vis luminescence spectrum of CS-MSNs under 980 nm NIR excitation (a), and photoluminescence spectra of CS-MSNs under Xe lamp excitation at 245 nm and 327 nm (b).

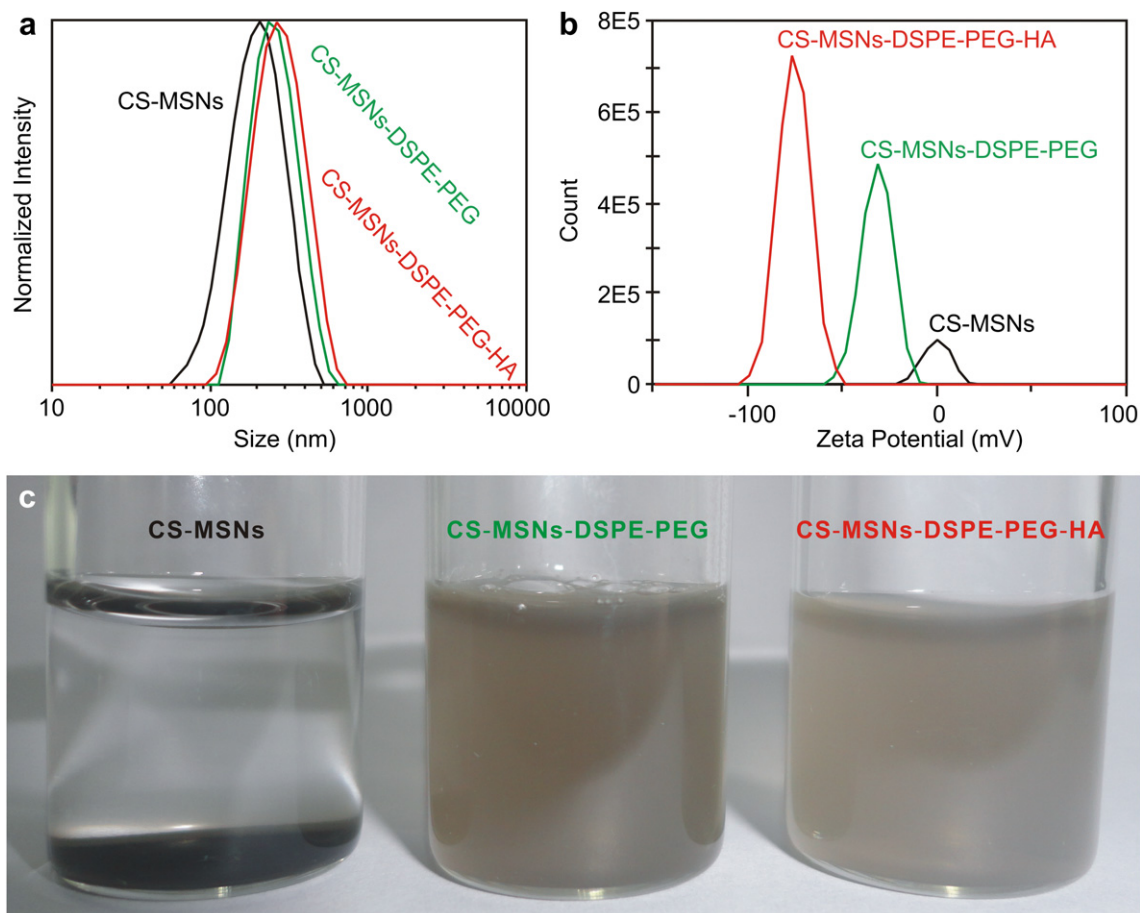


Fig. 6. Particle size distributions (a) by DLS technique, surface potentials (b) and aqueous suspendability (c) of CS-MSNs before and after bio-conjugation with DSPE-PEG and HA.

smaller pore sizes than the as-synthesized MSNs (inset of Fig. 4), which could result from the shrinkage of mesoporous walls during the high temperature treatment and the spatial occupation of carbon within mesopores. Even so, CS-MSNs still have a relatively high specific surface area of  $64 \text{ m}^2/\text{g}$  and a large pore volume of  $0.15 \text{ m}^3/\text{g}$ , which would be enough for CS-MSNs to load the adequate quantity of water-insoluble drugs as indicated by a relatively high CPT loading capacity ( $68 \text{ mg/g}$ ) compared with the values reported previously [36–38]. Besides, the most important is that the hydrophobicity of *in situ* formed carbon favors the adsorption and loading of water-insoluble drugs such as CPT. Moreover, the  $\pi$ – $\pi$  stacking between the graphite-like carbon and the insoluble drug CPT also can make contribution to drug adsorption [39]. Comparatively, the routine MSNs cannot load such amounts of water-insoluble drugs because of their strong hydrophilicity of inside and outside surfaces including abundant Si–OH and Si–O<sup>−</sup> groups. However, the graphite-like carbon derived during calcination in nitrogen flow was highly hydrophobic, and the condensation between Si–OH groups during calcination (as proved above by FTIR results) resulted in the great reduction in the hydrophilicity of silica [40], therefore CS-MSNs with good hydrophobicity could adsorb considerable water-insoluble drugs. Therefore, the present *in situ* carbonization method has been a success for the simultaneous generation of Si nanocrystals, protection of mesopore structure and loading water-insoluble drugs in MSNs.

Importantly, Si nanocrystals within CS-MSNs could create the NIR-to-Vis luminescence under the excitation of 980 nm NIR laser (Fig. 5) as expected, which is a very interesting advantage in bio-

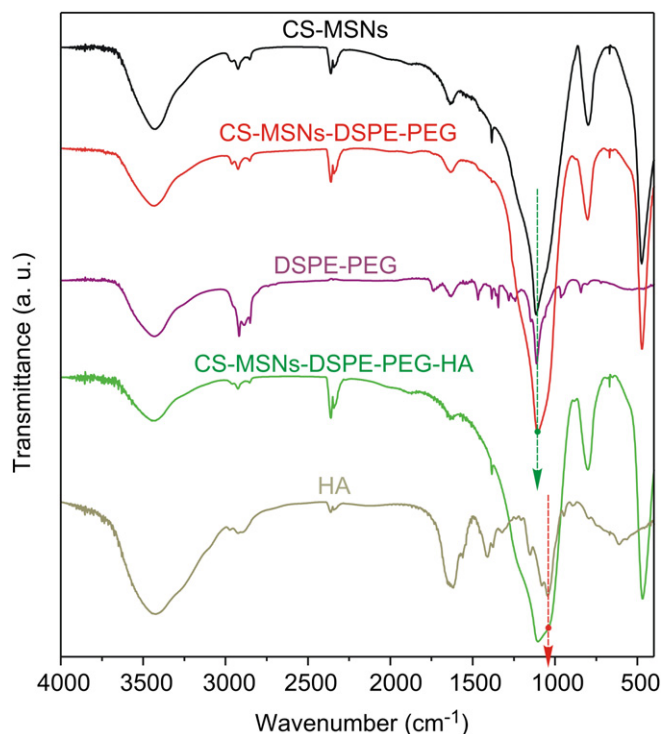


Fig. 7. FTIR spectra of CS-MSNs, CS-MSNs-DSPE-PEG, DSPE-PEG, CS-MSNs-DSPE-PEG-HA, and HA.

imaging applications and is also a significant advancement as compared with the UV-to-Vis luminescence of ODL-MSNs reported previously [29]. From Fig. 5a, two wide emission bands of CS-MSNs could be obtained in the visible region under 980 nm excitation, which should result from the multi-photon excitation and size-dependent luminescence characteristics of Si nanocrystals. Recently, Si nanocrystals have also been proved to be capable to generate NIR-to-Vis emission under multi-photon excitations, and the luminescence bands depend on crystal size [20,21,41]. To demonstrate this further, the photoluminescence was also excited by multiple frequencies, 245 nm and 327 nm corresponding to four-photon and three-photon energies of 980 nm excitation, respectively. As shown in Fig. 5a and b kind of broad-band emission at 300–700 nm was exhibited under 245 nm and 327 nm excitation, which was similar to that excited at 980 nm. This suggested that the NIR-to-Vis luminescence of CS-MSNs could be derived from the multi-photon excitation. The non-overlay between two emission bands of CS-MSNs for single-photon and multi-photon excitations reported in this work can be derived from a blue-shift phenomenon owing to the silicon@silica embedding structure

[42]. In addition, the broad-spectrum emission from blue to red in the visible region made CS-MSNs look yellow under 980 nm excitation, as shown directly by the photograph (Fig. S2) in the Supporting information. This NIR-to-Vis luminescence characteristic of CS-MSNs would greatly favor their biological imaging applications. Comparatively, UCNP generally exhibit narrow emission bands, but have also potential toxicity because usually containing rare-earth heavy elements. However, Si and silica have lower toxicity and better biocompatibility, therefore would be more appropriate to bio-applications.

### 3.2. Bio-conjugation of CS-MSNs

Good aqueous solubility and hemocompatibility are necessary for cargoes to escape from bio-barriers and then efficiently deliver drugs to lesion focus, and bio-conjugation and PEGylation are the predominant routes for inorganic nano-cargoes [43–45]. Therefore in the present work, the CPT-loaded CS-MSNs (CPT@CS-MSNs) were coated with a PEGylated phospholipid compound DSPE-PEG, as shown in Scheme 1, because this kind of phospholipid

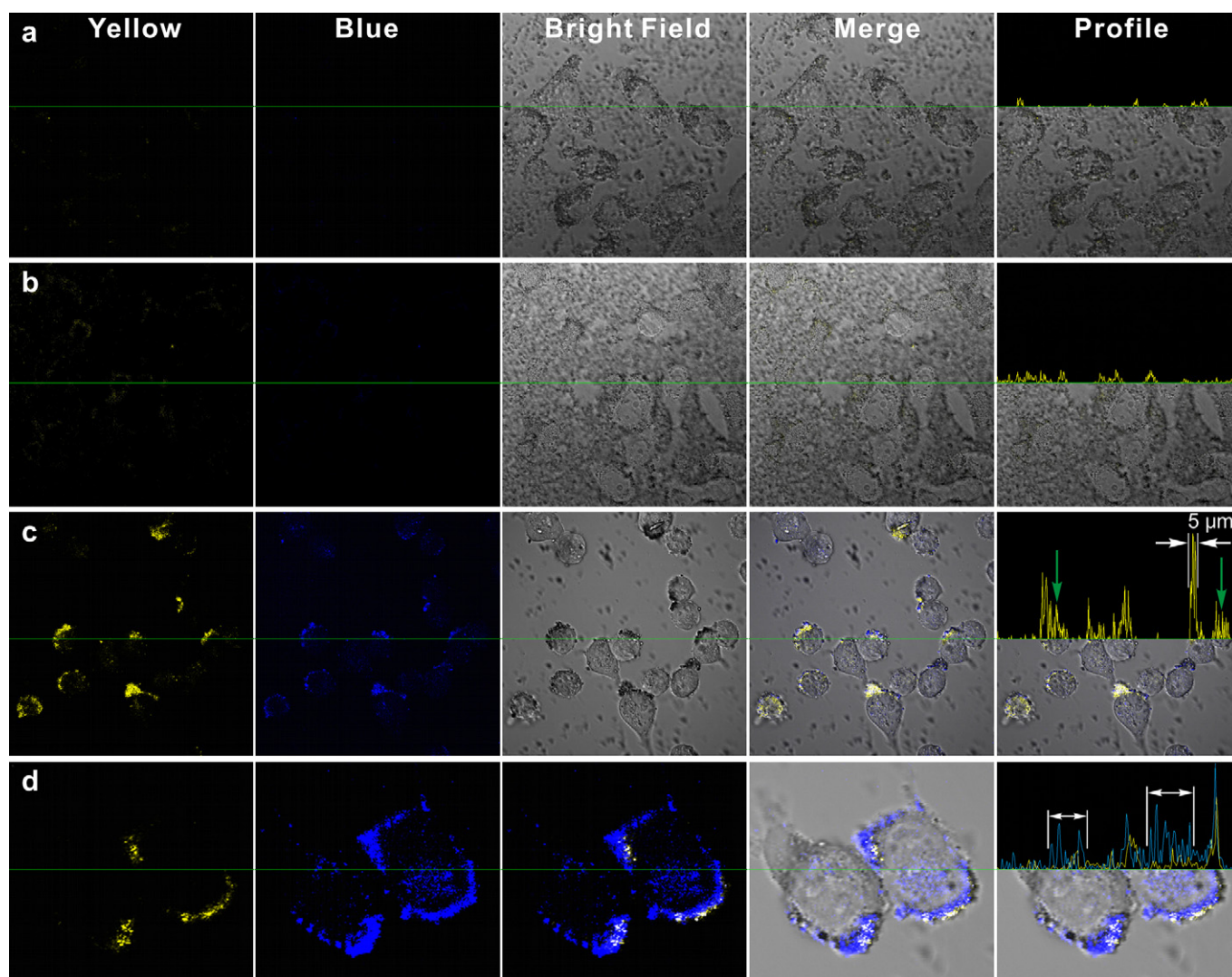


**Fig. 8.** The targeting, luminescence imaging and drug delivery behaviors of CPT@CS-MSNs-DSPE-PEG-HA to MDA-MB-468 cells (c, d), compared with these of L929 cells (a) and MCF-7 cells (b). Figures (d) are the high-magnification confocal images of MDA-MB-468 cells treated with CPT@CS-MSNs-DSPE-PEG-HA. Yellow and blue fluorescence signals represent the intracellular localization of CS-MSNs and CPT, respectively. Therefore, blue region beyond the reach of yellow fluorescence signals reflects intracellular release of blue CPT from yellow nanoparticles, as shown in Figures (d). Right profiles were collected by scanning cells in green line. Thereinto, yellow and blue signals reflect CS-MSNs and CPT, respectively. (For interpretation of the references to color in this figure legend, the reader is referred to the web version of this article.)

compounds is well recognized of good biocompatibility and membrane permeability [45–48]. In order to prevent the nanoparticles from aggregation, the as-synthesized MSNs were dispersed in water at a low concentration and then freeze-dried into powder. Therefore, CS-MSNs could still keep good dispersivity in spite of high temperature calcination, as indicated by narrow particle size distribution (Fig. 6a) measured by dynamic light scattering technique. Once CS-MSNs were completely dispersed under intensive stirring, their particle size distribution (Fig. 6a) and surface potential (Fig. 6b) were measured. Once stirring was withdrawn, CS-MSNs would flocculate in several minutes of static balancing owing to the poor water-solubility, as shown by Fig. 6c. After conjugation with DSPE-PEG, the suspendability of CPT@CS-MSNs in PBS was remarkably improved, as indicated visually in Fig. 6c, and both the sharp particle size distribution with an average hydrated diameter of  $260 \pm 86$  nm (Fig. 6a) and the negative surface potential of  $-31.2 \pm 8.5$  mV (Fig. 6b) were exhibited. These suggested the successful modification of DSPE-PEG on CPT@CS-MSNs (CPT@CS-MSNs-DSPE-PEG).

HA, a natural mucopolysaccharide of excellent biocompatibility and biodegradability, is the principal ligand of CD44 which is frequently overexpressed on rapidly dividing breast cancer cells, therefore is well qualified for the bio-conjugation of nano-cargoes for targeting drug delivery [49–52]. Therefore in order to gain the capability of targeting special cancer cells overexpressing CD44, CPT@CS-MSNs-DSPE-PEG was further conjugated with HA by an esterification reaction. As a result, excellent solubility/suspendability of the HA-conjugated CPT@CS-MSNs-DSPE-PEG (CPT@CS-MSNs-DSPE-PEG-HA) in PBS was achieved (Fig. 6c), and its particle size distribution was still kept sharp (Fig. 6a) in accordance with TEM imaging results (Fig. 1d), however, average hydrated size and surface potential increased to  $290 \pm 105$  nm and  $-75.2 \pm 8.5$  mV, respectively (Fig. 6a and b), reflecting the successful HA conjugation.

In addition, the successful bio-conjugation of CS-MSNs with DSPE-PEG and HA was also confirmed by FTIR measurements (Fig. 7). DSPE-PEG shows the strongest characteristic absorption band of C–O–C at  $1107\text{ cm}^{-1}$ , where the stretching band of Si–O–Si in CS-MSNs also resides. After conjugation with DSPE-PEG, the absorption intensity of CS-MSNs at  $1107\text{ cm}^{-1}$  is significantly enhanced taking the rocking band of Si–O–Si at  $470\text{ cm}^{-1}$  as the reference, as indicated by the green arrow. This suggests the successful conjugation of DSPE-PEG onto CS-MSNs. Similarly, the enhanced absorption at  $1050\text{ cm}^{-1}$  compared with the absorption at  $470\text{ cm}^{-1}$ , as indicated by the red arrow, suggests that HA had been well conjugated onto CS-MSNs-DSPE-PEG.

### 3.3. Cell-targeted drug delivery and NIR-to-vis luminescence imaging

Next, the cell targeting, intracellular drug delivery and luminescence imaging behaviors of the drug-encapsulated and bio-conjugated CS-MSNs were explored with representative normal cells (fibroblast L929 cells) and cancer cells (breast cancer MCF-7 and MDA-MB-468 cells). First, the CD44 contents on these representative cells were detected quantitatively by an enzyme-linked immunosorbent assay. The CD44 expression amount of MDA-MB-468 cells is measured to be as high as 1.94 ng/mL, however that of MCF-7 and L929 cells are only 0.27 ng/mL and 0.18 ng/mL, respectively, indicating that MDA-MB-468 cancer cells did over-express CD44 remarkably, however the CD44 excessive expression on MCF-7 cancer cells was very slight, as compared with L929 normal cells. To confirm the targetability and intracellular drug delivery of the constructed theranostic hierarchical nanostructure CPT@CS-MSNs-DSPE-PEG-HA, confocal imaging technology was used to observe cells after treatment with CPT@CS-MSNs-DSPE-

PEG-HA. As shown in Fig. 8, there were very few nanoparticles being internalized by L929 cells (Fig. 8a) due to the non-specific uptake, and slightly more but still limited nanoparticles being uptaken by MCF-7 cells (Fig. 8b) after incubation for 4 h, as indicated by yellow signals of confocal images and corresponding linear scanning profiles. However a large number of yellow fluorescent nanoparticles can be found enriched around the membranes of MDA-MB-468 cells with a  $5\text{ }\mu\text{m}$  extension toward the cytosol (as indicated by the white arrow in Fig. 8c) under the illumination by 980 nm laser, and there were also many nanoparticles internalized in the cytosol of MDA-MB-468 cells after the same treatment (Fig. 8c). Further, the representative profile of MDA-MB-468 cells indicated the cytosolic internalization of nanoparticles, as shown by green arrows in Fig. 8c. This indicates two facts: 1) the bio-conjugated CS-MSNs could indeed target and enter MDA-MB-468 cells actively, but neither MCF-7 nor L929 cells, owing to the targeting capability of HA molecules conjugated onto CS-MSNs to bind CD44 protein overexpressed on MDA-MB-468 cells specifically, as mentioned above [53,54]; 2) while targeting MDA-MB-468 cells, CS-MSNs could still image these cells with strong yellow fluorescence under 980 nm NIR excitation by a multi-photon excitation route, well inheriting their NIR-to-Vis luminescence characteristic as demonstrated above (Fig. 5). Furthermore, it can also be found that the nanoparticles uptaken by MDA-MB-468 cells can release CPT in these cells, as indicated by blue fluorescence signals spreading all over cells beyond the reach of nanoparticles in the yellow in Fig. 8c, which was further exhibited visually by high-magnification confocal images and was also indicated clearly by the white arrows in corresponding linear scanning profiles (Fig. 8d). As expected, these drug-encapsulated and bio-conjugated CS-MSNs selectively and efficiently killed MDA-MB-468 cells, but had insignificant effect on both MCF-7 cells and L929 cells (Fig. 9) and the cytotoxicity of free CPT is quite low in 24 h against three types of cells in the present conditions (Fig. S3a, Supporting information), most probably owing to low solubility of CPT. This should be attributed to the cell targeting and intracellular drug delivery/release behaviors as mentioned above. In addition, the carrier

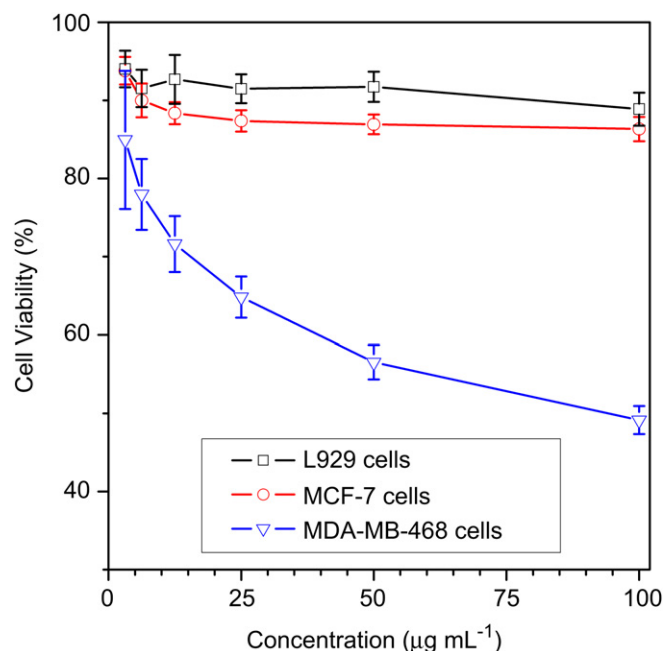


Fig. 9. Cytotoxicity of CPT@CS-MSNs-DSPE-PEG-HA against L929, MCF-7 and MDA-MB-468 cells.

shows very low cytotoxicity against three types of cells in the present conditions, as indicated by Fig. S3b in the Supporting information.

#### 4. Conclusions

CS-MSNs with carbon and Si nanocrystals encapsulated respectively in the mesopore channels and within mesoporous framework, has been constructed by a facile bottom-up self-assembly strategy combined with an *in situ* one-step carbonization/crystallization approach. Special silicon sources and high temperature calcination under inert atmosphere were employed to generate carbon species and silicon nanocrystals. Such a therapeutic platform integrates the advantages of well-defined morphology and monodispersed size, high payload of water-insoluble drugs and unique NIR-to-Vis luminescence imaging capability. The bio-conjugated CS-MSNs with DSPE-PEG and HA showed excellent dispersivity and could specifically target cancer cells overexpressing CD44, deliver water-insoluble drugs into these cells and consequently kill them effectively, and also fluorescently image them simultaneously in a unique NIR-to-Vis luminescence imaging fashion.

#### Acknowledgments

The authors thank L.L. Zhang, J.Q. Luo and Y. Yang for TEM, Raman and PL measurements, respectively. This work was financially supported by the National Nature Science Foundation of China (Grant Nos. 51102259, 51132009, 50823007 and 50972154), the Science and Technology Commission of Shanghai (Grant Nos. 10430712800, 11nm0505000, 11nm0506500), the Science Foundation for Youth Scholar of State Key Laboratory of High Performance Ceramics and Superfine Microstructures (Grant No. SKL201001).

#### Appendix. Supplementary data

Supplementary data associated with this article can be found, in the online version, at doi:10.1016/j.biomaterials.2012.02.056.

#### References

- [1] Sun DX. Nanotheranostics: integration of imaging and targeted drug delivery. *Mol Pharm* 2010;7:1879.
- [2] Bae KH, Chung HJ, Park TG. Nanomaterials for cancer therapy and imaging. *Mol Cells* 2011;31:295–302.
- [3] Xie J, Lee S, Chen XY. Nanoparticle-based theranostic agents. *Adv Drug Deliv Rev* 2010;62:1064–79.
- [4] Kim J, Piao Y, Hyeon T. Multifunctional nanostructured materials for multimodal imaging, and simultaneous imaging and therapy. *Chem Soc Rev* 2009;38:372–90.
- [5] Ambrogio MW, Thomas CR, Zhao YL, Zink JJ, Stoddart JF. Mechanized silica nanoparticles: a new frontier in theranostic nanomedicine. *Acc Chem Res* 2011;44:903–13.
- [6] He QJ, Shi JL. Mesoporous silica nanoparticles based nano drug delivery systems: synthesis, controlled drug release and delivery, pharmacokinetics and biocompatibility. *J Mater Chem* 2011;21:5845–55.
- [7] Kim J, Kim HS, Lee N, Kim T, Kim H, Yu T, et al. Multifunctional uniform nanoparticles composed of a magnetite nanocrystal core and a mesoporous silica shell for magnetic resonance and fluorescence imaging and for drug delivery. *Angew Chem Int Ed* 2008;47:8438–41.
- [8] Kim J, Lee JE, Lee J, Yu JH, Kim BC, An K, et al. Magnetic fluorescent delivery vehicle using uniform mesoporous silica spheres embedded with monodisperse magnetic and semiconductor nanocrystals. *J Am Chem Soc* 2006;128:688–9.
- [9] Taylor KML, Kim JS, Rieter WJ, An HY, Lin WL, Lin WB. Mesoporous silica nanospheres as highly efficient MRI contrast agents. *J Am Chem Soc* 2008;130:2154–5.
- [10] Lin YS, Wu SH, Hung Y, Chou YH, Chang C, Lin ML, et al. Multifunctional composite nanoparticles: magnetic, luminescent, and mesoporous. *Chem Mater* 2006;18:5170–2.
- [11] Hu XG, Zrazhevskiy P, Gao XH. Encapsulation of single quantum dots with mesoporous silica. *Ann Biomed Eng* 2009;37:1960–6.
- [12] Yang Y, Qu Y, Zhao J, Zeng Q, Ran Y, Zhang Q, et al. Fabrication of and drug delivery by an upconversion emission nanocomposite with monodisperse LaF<sub>3</sub>:Yb, Er core/mesoporous silica shell structure. *Eur J Inorg Chem* 2010;33:5195–9.
- [13] Yang PP, Quan ZW, Hou ZY, Li CX, Kang XJ, Cheng ZY, et al. A magnetic, luminescent and mesoporous core-shell structured composite material as drug carrier. *Biomaterials* 2009;30:4786–95.
- [14] Wang C, Tao HQ, Cheng L, Liu Z. Near-infrared light induced in vivo photodynamic therapy of cancer based on upconversion nanoparticles. *Biomaterials* 2011;32:6145–54.
- [15] Xu H, Cheng L, Wang C, Ma XX, Li YG, Liu Z. Polymer encapsulated upconversion nanoparticle/iron oxide nanocomposites for multimodal imaging and magnetic targeted drug delivery. *Biomaterials* 2011;32:9364–73. <http://www.sciencedirect.com/science/article/pii/S0142961211010015>.
- [16] Wang C, Cheng L, Liu Z. Drug delivery with upconversion nanoparticles for multi-functional targeted cancer cell imaging and therapy. *Biomaterials* 2011;32:1110–20.
- [17] Xing HY, Bu WB, Zhang SJ, Zheng XP, Li M, Chen F, et al. Multifunctional nanopores for upconversion fluorescence, MR and CT trimodal imaging. *Biomaterials* 2012;33:1079–89.
- [18] Zhou J, Liu Z, Li FY. Upconversion nanophosphors for small-animal imaging. *Chem Soc Rev* 2012;41:1323–49.
- [19] Erogbogbo F, Yong KT, Roy I, Xu GX, Prasad PN, Swihart MT. Biocompatible luminescent silicon quantum dots for imaging of cancer cells. *ACS Nano* 2008;2:873–8.
- [20] Tu CQ, Ma XC, Pantazis P, Kauzlarich SM, Louie AY. Paramagnetic, silicon quantum dots for magnetic resonance and two photon imaging of macrophages. *J Am Chem Soc* 2010;132:2016–23.
- [21] He GS, Zheng QD, Yong KT, Erogbogbo F, Swihart MT, Prasad PN. Two- and three-photon absorption and frequency upconverted emission of silicon quantum dots. *Nano Lett* 2008;8:2688–92.
- [22] Brigger I, Dubernet C, Couvreur P. Nanoparticles in cancer therapy and diagnosis. *Adv Drug Deliv Rev* 2002;54:631–51.
- [23] Rosenholm JM, Meinander A, Peulhu E, Niemi R, Eriksson JE, Sahlgren C, et al. Targeting of porous hybrid silica nanoparticles to cancer cells. *ACS Nano* 2009;3:197–206.
- [24] Lebreit V, Raehm L, Durand JO, Smaïhi M, Werts MHV, Blanchard-Desce M, et al. Folic acid-targeted mesoporous silica nanoparticles for two-photon fluorescence. *J Biomed Nanotechnol* 2010;6:176–80.
- [25] Tsai CP, Chen CY, Hung Y, Chang FH, Mou CY. Monoclonal antibody-functionalized mesoporous silica nanoparticles (MSN) for selective targeting breast cancer cells. *J Mater Chem* 2009;19:5737–43.
- [26] Brevet D, Bobo MG, Raehm L, Richeter S, Hocine O, Amro K, et al. Mannose-targeted mesoporous silica nanoparticles for photodynamic therapy. *Chem Commun* 2009;12:1475–7.
- [27] Wells AS. On the perils of unexpected silane generation. *Org Process Res Dev* 2010;14:484.
- [28] Guo LM, Li JT, Zhang LX, Li JB, Li YS, Yu CC, et al. A facile route to synthesize magnetic particles within hollow mesoporous spheres and their performance as separable Hg<sup>2+</sup> adsorbents. *J Mater Chem* 2008;18:2733–8.
- [29] He QJ, Shi JL, Cui XZ, Wei CY, Zhang LX, Wu W, et al. Synthesis of oxygen-deficient luminescent mesoporous silica nanoparticles for synchronous drug delivery and imaging. *Chem Commun* 2011;47:7947–9.
- [30] Kim H, Cho J. Superior lithium electroactive mesoporous Si/carbon core-shell nanowires for lithium battery anode material. *Nano Lett* 2008;8:3688–91.
- [31] Li YS, Ba A. Spectroscopic studies of triethoxysilane sol-gel and coating process. *Spectrochim Acta Part A* 2008;70:1013–9.
- [32] Vella E, Buscarino G, Vaccaro G, Boscaïno R. Structural organization of silanol and silicon hydride groups in the amorphous silicon dioxide network. *Eur Phys J B* 2011;83:47–52.
- [33] Hessel CM, Henderson EJ, Veinot JGC. Hydrogen silsesquioxane: a molecular precursor for nanocrystalline Si–SiO<sub>2</sub> composites and freestanding hydride-surface-terminated silicon nanoparticles. *Chem Mater* 2006;18:6139–46.
- [34] Cohen Y, Hatton B, Míguez H, Coombs N, Fournier-Bidoz S, Grey J, et al. Spin-on nanostructured silicon–silica film displaying room-temperature nanosecond lifetime photoluminescence. *Adv Mater* 2003;15:572–6.
- [35] Cohen Y, Landskron K, Tétreault N, Fournier-Bidoz S, Hatton B, Ozin G. A silicon–silica nanocomposite material. *Adv Funct Mater* 2005;15:593–602.
- [36] Lu J, Liong M, Zink JJ, Tamanoi F. Mesoporous silica nanoparticles as a delivery system for hydrophobic anticancer drugs. *Small* 2007;3:1341–6.
- [37] Lu J, Liong M, Li ZX, Zink JJ, Tamanoi F. Biocompatibility, biodistribution, and drug-delivery efficiency of mesoporous silica nanoparticles for cancer therapy in animals. *Small* 2010;6:1794–805.
- [38] He QJ, Gao Y, Zhang LX, Bu WB, Chen HR, Li YP, et al. One-pot self-assembly of mesoporous silica nanoparticle-based pH-responsive anti-cancer nano drug delivery system. *J Mater Chem* 2011;21:15190–2.
- [39] Liu Z, Robinson JT, Sun XM, Dai HJ. PEGylated nanographene oxide for delivery of water-insoluble cancer drugs. *J Am Chem Soc* 2008;130:10876–7.
- [40] Cauvel A, Brunel D, Renzo FD, Garrone E, Fubini B. Hydrophobic and hydrophilic behavior of micelle-templated mesoporous silica. *Langmuir* 1997;13:2773–8.

- [41] Belomoin G, Therrien J, Smith A, Rao S, Twisten R, Chaieb S, et al. Observation of a magic discrete family of ultrabright Si nanoparticles. *Appl Phys Lett* 2002; 80:841–3.
- [42] Zou J, Baldwin RK, Pettigrew KA, Kauzlarich SM. Solution synthesis of ultrastable luminescent siloxane-coated silicon nanoparticles. *Nano Lett* 2004;4:1181–6.
- [43] Kumar R, Roy I, Ohulchanskyy TY, Goswami LN, Bonoiu AC, Bergey EJ, et al. Covalently dye-linked, surface-controlled, and bioconjugated organically modified silica nanoparticles as targeted probes for optical imaging. *ACS Nano* 2008;2:449–56.
- [44] He QJ, Zhang JM, Shi JL, Zhu ZY, Zhang LX, Bu WB, et al. The effect of PEGylation of mesoporous silica nanoparticles on nonspecific binding of serum proteins and cellular responses. *Biomaterials* 2010;31:1085–92.
- [45] Liu Z, Tabakman SM, Chen Z, Dai HJ. Preparation of carbon nanotube bioconjugates for biomedical applications. *Nat Protoc* 2009;4:1372–81.
- [46] Liu JW, Stace-Naughton A, Jiang XM, Brinker CJ. Porous nanoparticle supported lipid bilayers (Protocells) as delivery. *J Am Chem Soc* 2009;131:1354–5.
- [47] Wang LS, Wu LC, Lu SY, Chang LL, Teng IT, Yang CM, et al. Biofunctionalized phospholipid-capped mesoporous silica nanoshuttles for targeted drug delivery: improved water suspensibility and decreased nonspecific protein binding. *ACS Nano* 2010;4:4371–9.
- [48] Ashley CE, Carnes EC, Phillips GK, Padilla D, Durfee PN, Brown PA, et al. The targeted delivery of multicomponent cargos to cancer cells by nanoporous particle-supported lipid bilayers. *Nat Mater* 2011;10:476.
- [49] Knudson W. Tumor-associated hyaluronan: providing an extracellular matrix that facilitates invasion. *Am J Pathol* 1996;148:1721–6.
- [50] Choi KY, Min KH, Yoon HY, Kim K, Park JH, Kwon IC, et al. PEGylation of hyaluronic acid nanoparticles improves tumor targetability in vivo. *Biomaterials* 2011;32:1880–9.
- [51] Ossipov DA. Nanostructured hyaluronic acid-based materials for active delivery to cancer. *Expert Opin Drug Del* 2010;7:681–703.
- [52] Kim KS, Hur W, Park SJ, Hong SW, Choi JE, Goh EJ, et al. Bioimaging for targeted delivery of hyaluronic acid derivatives to the livers in cirrhotic mice using quantum dots. *ACS Nano* 2010;4:3005–14.
- [53] Affy A, Purnell P, Nguyen L. Role of CD44s and CD44v6 on human breast cancer cell adhesion, migration, and invasion. *Exp Mol Pathol* 2009;86:95–100.
- [54] Katagiri YU, Sleeman J, Fujii H, Herrlich P, Hotta H, Tanaka K, et al. CD44 variants but not CD44s cooperate with b1-containing integrins to permit cells to bind to osteopontin independently of arginine-glycine-aspartic acid, thereby stimulating cell motility and chemotaxis. *Cancer Res* 1999;59:219–26.